Potentials Near a Curved Anode Edge in a PEM Fuel Cell: Analytical Solution for Placing a Reference Electrode

A. A. Kulikovsky[a,b,*,z]

[a]*Forschungszentrum Juelich GmbH, Institute of Energy and Climate Research, IEK-3: Electrochemical Process Engineering, D-52425 Jülich, Germany*
[b]*Lomonosov Moscow State University, Research Computing Center, 119991 Moscow, Russia*

We consider a PEM fuel cell with concentric circular electrodes: the small anode and the large cathode. A model for in-plane distributions of the cathode overpotential η_c and the membrane potential Φ in the anode-free region of the cell is developed. Mathematically, the problem reduces to the axially symmetric Poisson–Boltzmann equation for η_c. An approximate analytical solution shows that $|\eta_c|$ exhibits rapid decay to zero with the radius, while $|\Phi|$ grows to the value of $|\eta_c^0|$, the cathode overpotential in the working domain of the cell. For typical η_c^0, the radial shape of η_c far from the anode edge only weakly depends on η_c^0; this effect is analogous to Debye screening in plasmas. The smaller the anode radius, the faster Φ approaches η_c^0 with the distance from the anode. It follows, that a reference electrode for measuring the cathode overpotential in the working area can be placed at a small distance from the curved anode edge.

Performance of a polymer electrolyte membrane fuel cell (PEMFC) is determined by overpotentials driving the electrochemical reactions on either side of the cell. One of the most useful techniques for measuring the half-cell overpotentials is a method of reference electrode (RE). A typical schematic of a cell with the RE is depicted in Figure 1a. The hydrogen-fed RE is located at a certain distance L_{gap} from the aligned anode and cathode edges. Neglecting the potential loss for the hydrogen oxidation/evolution reactions, the potential of the RE is equal to the membrane potential Φ at the point of the RE location. If the distance L_{gap} is large enough, the measured Φ corresponds to the membrane potential at some point along the y-axis between the anode and cathode in the working cell area (Figure 1a). Measuring Φ and the electrode potentials allows one to separate the anode and cathode overpotentials in the cell.[1,2] Further, RE enables to perform electrochemical impedance spectroscopy between the RE and each of the cell electrodes; this technique has been widely used in SOFC studies.[3–6]

The problem with the system in Figure 1a is that even a small misalignment of the anode and cathode edges may strongly distort Φ at the RE location. This problem has been intensively studied for different types of fuel cells.[3–5,7] Recently, a design free from this drawback has been suggested[8] (Figure 1b). Here, the cathode is continuous and the RE is located at a distance L_{gap} from the straight anode edge. The absence of the cathode edge eliminates the misalignment problem. It has been shown, that for the design in Figure 1b, L_{gap} must satisfy to the condition[8]

$$L_{gap} \gtrsim 3\sqrt{\frac{\sigma_m b_{ox} l_m}{2 j_{ox}^0}} \qquad [1]$$

Here, σ_m is the membrane proton conductivity, b_{ox} is the Tafel slope of the oxygen reduction reaction (ORR), l_m is the membrane thickness, j_{ox}^0 is the superficial exchange current density (A cm^{-2}) of the cathode in the working cell area. With typical cell parameters (Table I), L_{gap} appears to be on the order of several centimeters. For a typical laboratory-size cell of about 10×10 cm^2, this value of L_{gap} is quite large. Below, we show that a *curved* anode edge enables significant reduction of L_{gap} not sacrificing the accuracy of measurements.

We report a model for the radial distribution of the membrane potential Φ and the cathode overpotential η_c in the anode-free area of a cell with the small circular anode and the large cathode. An approximate analytical solution of the problem is derived. It shows that far from the anode edge, the radial shape of the cathode overpotential

$\eta_c(r)$ only weakly depends of the value η_c^0 at the edge, provided that $|\eta_c^0|$ is sufficiently large. This effect is quite analogous to Debye screening in plasmas. Further, analytical solution allows us to calculate the width of the gap between the curved anode edge and the RE for measuring the cathode overpotential in the working domain of the cell. In a certain range of anode radii, the smaller the radius of the anode edge, the closer to the edge can be located the RE.

Model

The model below is close in spirit to the model[8] for the straight anode edge above the infinite cathode (Figure 1b). Here, however, we consider a system of concentric circular electrodes depicted in Figure 2. Let the radii of the anode and cathode electrodes be R_a and R_c, respectively; we will assume that $R_c \to \infty$. In the following, the
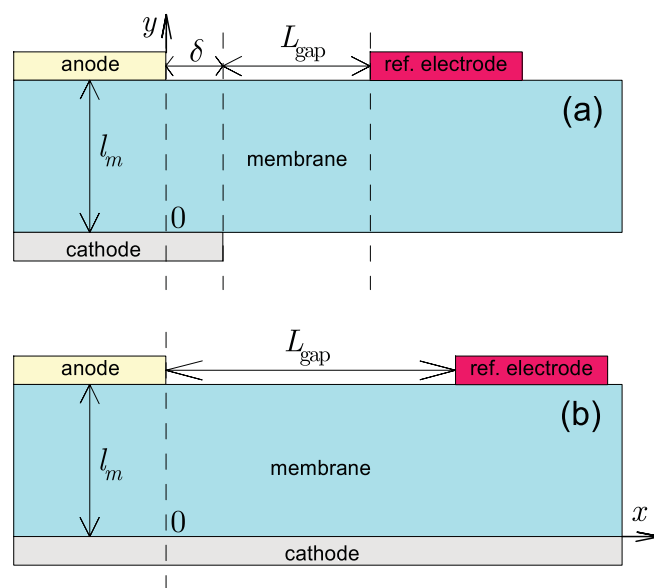

Figure 1. Schematic of the fuel cell with the reference electrode. (a) A conventional scheme; note that a small misalignment δ of the working anode and cathode edges strongly distort the membrane potential at the reference electrode location. (b) A scheme.[8] Here, the reference electrode is located at a large distance L_{gap} from the anode edge, while the cathode is continuous.

*Electrochemical Society Active Member.
zE-mail: A.Kulikovsky@fz-juelich.de

Table I. The base-case physical parameters for the calculations.

ORR exchange current density j_{ox}^0, A cm^{-2}	10^{-6}
ORR equilibrium potential E_{ORR}^{eq}, V	1.23
ORR Tafel slope b_{ox}, V	0.03
HOR exchange current density in the working domain j_{hy}^0, A cm^{-2}	1.0
HOR Tafel slope b_{hy}, V	0.015
Membrane proton conductivity σ_m, Ω^{-1} cm^{-1}	0.1
Membrane thickness l_m, cm	0.005 (50 μm)
Cell potential ϕ_c, V	0.82642
Mean current density in the working domain J, A cm^{-2}	0.6
Parameter κ	$1.826 \cdot 10^{-3}$

cell domains $r \leq R_a$ and $R_a < r < \infty$ will be referred to as the working and anode-free domains, respectively (Figure 2).

Our goal is understanding the distribution of currents and potentials in this system. The main variable in this problem is the membrane potential Φ, which obeys to the Poisson equation

$$\frac{1}{r}\frac{\partial}{\partial r}\left(r\frac{\partial \Phi}{\partial r}\right) + \frac{\partial^2 \Phi}{\partial z^2} = 0 \qquad [2]$$

Infinite cathode means that the radial extent of the problem R_c is by several orders of magnitude larger, than the membrane thickness (the exact criterium is given below). This allows us to approximate the second derivative along z in Eq. 2 by the difference of proton currents coming in and out of the membrane,[9] which yields

$$\frac{1}{r}\frac{\partial}{\partial r}\left(r\frac{\partial \Phi}{\partial r}\right) = \frac{j_c - j_a}{\sigma_m L_m} \qquad [3]$$

Here j_a and j_c are the proton current densities at the anode and the cathode side of the membrane, respectively.

In a well-humidified membrane, variation of Φ along z is close to linear, and hence the quasi-2D approximation of Eq. 3 works well everywhere, except a small region in the vicinity of the anode edge. Close to the anode edge, a fully 2D distribution of Φ forms. Numerical calculations of Adler et al.[4] show that in the system with the straight anode edge, this 2D-domain extends to the distance on the order of l_m from the edge. In the axially symmetric system, we may expect even smaller 2D domain. Thus, the radial distributions reported below may be not accurate in a ring of a width of l_m just outside the anode edge. However, of largest interest is the behavior of the potentials outside this ring, on a large radial distance from the anode edge.

Further, j_a and j_c are assumed to obey the approximate Butler–Volmer kinetics

$$j_a = 2j_{hy}\sinh\left(\frac{\eta_a}{b_{hy}}\right), \qquad [4]$$

$$j_c = 2j_{ox}\sinh\left(-\frac{\eta_c}{b_{ox}}\right), \qquad [5]$$

where j_{hy} and j_{ox} are the superficial exchange current densities of the anode catalyst layer (ACL) and the cathode catalyst layer (CCL), respectively, η_a and η_c are the local anode and cathode overpotentials, and b_{hy} and b_{ox} are the corresponding Tafel slopes. The approximate
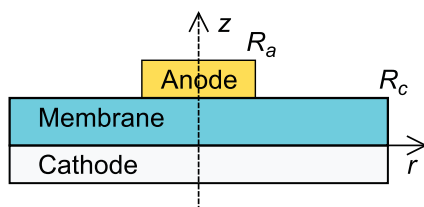

Figure 2. Schematic of the fuel cell with the concentric circular anode and cathode.

form 5 of the Butler–Volmer equation allows us to analyze a smooth transition from large to small current densities in the anode-free domain, which is a feature of this problem. Eq. 5 reduces to the standard Butler–Volmer equation if the transfer coefficient α of the ORR rate-determining step is 1/2. With another values of α, Eq. 5 is approximate in the region of $\eta_c \simeq b_{ox}$, and it reduces to the exact asymptotics for $\eta_c \ll b_{ox}$ and $\eta_c \gg b_{ox}$. Indeed, for $\eta_c \gg b_{ox}$, the reverse reaction is negligible, while for $\eta_c \ll b_{ox}$, the ORR kinetics is linear, and hence in both these limits, the Buler–Volmer equation and Eq. 5 lead to the same form of the ORR rate. Note that we assume that the transport losses in the electrodes are small and hence the dependencies on reactant concentrations are included in j_{hy} and j_{ox}.

The half-cell overpotentials are given by

$$\eta_a = \phi_a - \Phi - E_{HOR}^{eq}, \qquad [6]$$

$$\eta_c = \phi_c - \Phi - E_{ORR}^{eq}, \qquad [7]$$

where ϕ_a and ϕ_c are the anode and the cathode potentials, and $E_{HOR}^{eq} = 0$ and $E_{ORR}^{eq} = 1.23$ V are the equilibrium potentials of the respective half-cell reaction. We will assume that the anode is grounded ($\phi_a = 0$) and, hence, ϕ_c is the cell potential.

Substituting Eqs. 4–7 into Eq. 3 and introducing dimensionless variables

$$\tilde{r} = \frac{r}{l_m}, \quad \tilde{j} = \frac{jl_m}{\sigma_m b_{ox}}, \quad \tilde{\Phi} = \frac{\Phi}{b_{ox}}, \quad \tilde{\phi} = \frac{\phi}{b_{ox}}, \quad \tilde{b}_{hy} = \frac{b_{hy}}{b_{ox}}, \quad [8]$$

we come to

$$\frac{1}{\tilde{r}}\frac{d}{d\tilde{r}}\left(\tilde{r}\frac{d\tilde{\Phi}}{d\tilde{r}}\right) = 2\tilde{j}_{ox}^0\sinh\left(-\tilde{\phi}_c + \tilde{\Phi} + \tilde{E}_{ORR}^{eq}\right)$$
$$- 2\tilde{j}_{hy}^0 H(\tilde{R}_a - \tilde{r})\sinh(-\tilde{\Phi}/\tilde{b}_{hy}). \qquad [9]$$

Here, the superscript 0 indicates the value in the center of the working domain ($\tilde{r} = 0$) and H is the Heaviside function, which equals 1 in the working domain and zero in the anode-free domain. The absence of the anode catalyst outside the working domain is modeled as zero exchange current density of the hydrogen oxidation reaction (HOR).

Figure 3 shows the anode 4 and the cathode 5 current densities resulting from numerical solution of the problem 9 with the boundary conditions $\tilde{\Phi}(0) = \tilde{\Phi}_0$, $\partial\tilde{\Phi}/\partial\tilde{r}|_{\tilde{r}=\infty} = 0$. At the anode edge, a *current double layer* arises[10] (Figure 3b), which is analogous to a charged double layer at the surface of a solid charged particle in plasmas. The current double layer determines the shape of the cathode overpotential in the anode-free domain, as discussed below.

In the remainder of this work we will be interested in the distributions of Φ and η_c in the anode-free domain. In this region, production of current on the anode side vanishes, and Eq. 9 simplifies to

$$\frac{1}{\tilde{r}}\frac{d}{d\tilde{r}}\left(\tilde{r}\frac{d\tilde{\Phi}}{d\tilde{r}}\right) = 2\tilde{j}_{ox}^0\sinh\left(-\tilde{\phi}_c + \tilde{\Phi} + \tilde{E}_{ORR}^{eq}\right) \qquad [10]$$

It is convenient to rewrite this equation in terms of the cathode overpotential 7, which in the dimensionless variables is

$$\tilde{\eta}_c = \tilde{\phi}_c - \tilde{\Phi} - \tilde{E}_{ORR}^{eq} \qquad [11]$$

Substituting this into Eq. 10, we get

$$\frac{1}{\tilde{r}}\frac{d}{d\tilde{r}}\left(\tilde{r}\frac{d\tilde{\eta}_c}{d\tilde{r}}\right) = \kappa^2\sinh\tilde{\eta}_c \qquad [12]$$

where

$$\kappa = \sqrt{2\tilde{j}_{ox}^0} \qquad [13]$$

is the inverse dimensionless Debye length: $\kappa = \tilde{\lambda}_D^{-1}$. In dimensional form, the Debye length in this problem is given by

$$\lambda_D = \sqrt{\frac{\sigma_m b_{ox} l_m}{2 j_{ox}^0}} \qquad [14]$$

The physical meaning of λ_D is discussed in Debye screening section.
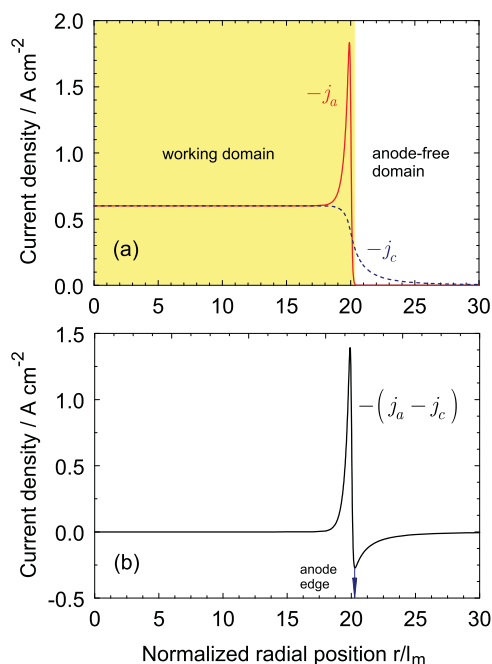
Figure 3. The anode j_a and cathode j_c current densities at the edge of the circular anode of the radius $\tilde{R}_a = 20$. For numerical calculation, the Heaviside function in Eq. 9 was smoothed, which is equivalent to the effective anode radius of $\tilde{R}_a \simeq 20.2$. Parameters for the calculation are listed in Table I. Note a large peak of the anode current at the edge of the electrode. Note also a "double layer" structure of the difference $j_a - j_c$, which appears on the right side of Eq. 9.

Analytical Solution

The problem for the straight anode edge above an infinite cathode leads to Eq. 12 with the second derivative in Cartesian coordinates $d^2\tilde{\eta}_c/dx^2$ on the left side.[8] It has been shown, that in PEM fuel cells, due to a very high exchange current density of the HOR, $\tilde{\eta}_c$ at the straight anode edge is very close to its value in the "bulk" area of the working domain.[8] Thus, in axial geometry, we may also expect that $\tilde{\eta}_c(\tilde{R}_a) \simeq \tilde{\eta}_c^0$, where $\tilde{\eta}_c^0 \equiv \tilde{\eta}_c(0)$ is the ORR overpotential at the axis of symmetry; numerical tests confirm this assumption. This allows us to exclude the working domain from consideration by fixing $\tilde{\eta}_c(\tilde{R}_a) = \tilde{\eta}_c^0$ at the anode edge. With this, the boundary conditions to Eq. 12 are

$$\tilde{\eta}_c(\tilde{R}_a) = \tilde{\eta}_c^0, \qquad \left.\frac{d\tilde{\eta}_c}{d\tilde{r}}\right|_{\tilde{r}=\infty} = 0 \qquad [15]$$

The second equation means zero in-plane proton current through the cathode edge. Validity of the infinite cathode approximation is guar-

anteed if

$$\kappa \tilde{R}_c \gg 1. \qquad [16]$$

Note, however, that Eq. 16 is redundant; a more accurate condition is discussed below.

The idea of the solution technique used here is as following. Close to the anode edge, the ORR rate dominates, which allows us to replace the sinh-function in Eq. 12 by the leading ORR exponent. The domain where this simplification works will be referred to as the ORR-dominated domain, as for $|\tilde{\eta}_c| > 2$, the cathode reaction is shifted to oxidation and the rate of the reverse reaction is small. Mathematically, this situation is equivalent to the dominance of positively charged species in the plasma close to the surface of a negatively charged macroscopic rod. Far from the anode, the rates of the forward and reverse reaction are nearly equal, and the sinh-function in Eq. 12 reduces to the linear dependence. Formally, this domain is equivalent to a quasineutral region in plasmas. Matching of the ORR-dominated and "quasineutral" solutions is performed by extending these solutions to the point, where $|\tilde{\eta}_c| = 1$.

Let the current density in the working domain be sufficiently large, i.e, $|\tilde{\eta}_c^0| \geq 2$. In the dimensional form this means that $|\eta_c^0| \geq 2b_{ox} \simeq 100$ mV, a condition, which in PEMFCs holds already at the cell current density of about 0.01 mA cm^{-2}. Then, in the vicinity of the anode edge, we can retain only the leading exponent in the expression for sinh-function in Eq. 12. Noting that $\tilde{\eta}_c < 0$, Eq. 12 in the ORR-dominated domain simplifies to

$$\frac{1}{\tilde{r}}\frac{d}{d\tilde{r}}\left(\tilde{r}\frac{d\tilde{\eta}_c}{d\tilde{r}}\right) = -\frac{\kappa^2}{2}\exp(-\tilde{\eta}_c) \qquad [17]$$

Introducing the *positive* overpotential

$$\tilde{\eta}_c^+ = -\tilde{\eta}_c > 0,$$

for $\tilde{\eta}_c^+$ we find an equation

$$\frac{1}{\tilde{r}}\frac{d}{d\tilde{r}}\left(\tilde{r}\frac{d\tilde{\eta}_c^+}{d\tilde{r}}\right) = \frac{\kappa^2}{2}\exp(\tilde{\eta}_c^+), \quad \tilde{\eta}_c^+(\tilde{R}_a) = \tilde{\eta}_c^{+,0}, \qquad [18]$$

where $\tilde{\eta}_c^{+,0} = -\tilde{\eta}_c^0 > 0$. A general solution to the problem 18 is

$$\tilde{\eta}_{c,S}^+ = \ln\left\{\frac{4A^2}{\kappa^2\tilde{r}^2}\left(1 + \tan^2\left[A\ln\left(\frac{\kappa\tilde{r}}{B}\right)\right]\right)\right\}, \quad \tilde{\eta}_{c,S}^+ \gg 1 \qquad [19]$$

where A and B are constants to be determined from the boundary and matching conditions. Note that the subscript S marks the short-range solution, valid in the vicinity of the anode edge.

Far from the anode edge, we have $\tilde{\eta}_c^+ \ll 1$, and the sinh-function on the right side of 12 can be expanded in Taylor series. With this, Eq. 12 simplifies to

$$\frac{1}{\tilde{r}}\frac{d}{d\tilde{r}}\left(\tilde{r}\frac{d\tilde{\eta}_c^+}{d\tilde{r}}\right) = \kappa^2\tilde{\eta}_c^+, \quad \left.\frac{d\tilde{\eta}_c^+}{d\tilde{r}}\right|_{\tilde{r}=\infty} = 0 \qquad [20]$$

where the boundary condition expresses zero in-plane proton current at the cathode edge. Solution to Eq. 20 is

$$\tilde{\eta}_{c,L}^+ = CK_0(\kappa\tilde{r}) \qquad [21]$$

where K is the modified Bessel function of the second kind and C is the constant to be determined from the matching conditions. The subscript L marks the long-range solution, valid far from the anode edge.

To fill the "gap" in the range of $\tilde{\eta}_c^+ \simeq 1$, we extend Eq. 19 down to $\tilde{\eta}_c^+ = 1$, and Eq. 21 up to $\tilde{\eta}_c^+ = 1$. Let the radius where $\tilde{\eta}_c^+ = 1$ be $\tilde{R}_1$:

$$\tilde{\eta}_c^+(\tilde{R}_1) = 1$$

Setting $\tilde{r} = \tilde{R}_1$ in Eq. 21, we get a relation for the constant C; expressing C from this relation and substituting the result to 21, we obtain

$$\tilde{\eta}_{c,L}^+ = \frac{K_0(\kappa\tilde{r})}{K_0(\kappa\tilde{R}_1)} \qquad [22]$$

Formally, Eq. 12 section

Formally, Eq. 12 is a Poisson–Boltzmann (PB) equation. Quite analogous equations arise in the theory of a diffuse double layer at the metal/electrolyte interface (Gouy–Chapman model[11,12]), and in the physics of charged macroscopic solid particles in plasmas.[13] The ORR rate in the Butler–Volmer term on the right side of Eq. 12 plays a role of a positive charge and the rate of the reverse reaction of water electrolysis in this term is equivalent to a negative charge in plasmas.

The main difference with the Gouy–Chapman problem for the planar diffuse double layer is axial symmetry of Eq. 12. Dyachkov[13] published analytical solution to Eq. 12 in the form of an infinite series. Zholkovskij et al.[14] derived matched asymptotic solution for the PB equation with spherical symmetry. Below, we employ a simple matching technique which leads to an accurate approximate analytical result.

The solutions 19 and 22 contain the three constants A, B and $\tilde{R}_1$ to be determined. The first relation between these constants is obtained by setting $\tilde{r} = \tilde{R}_1$ in Eq. 19:

$$\ln\left\{\frac{4A^2}{\kappa^2 \tilde{R}_1^2}\left(1 + \tan^2\left[A\ln\left(\frac{\kappa \tilde{R}_1}{B}\right)\right]\right)\right\} = 1 \qquad [23]$$

Another relation results from continuity of the first derivatives of 19 and 22 at $\tilde{r} = \tilde{R}_1$

$$\frac{K_1\left(\kappa \tilde{R}_1\right)}{K_0\left(\kappa \tilde{R}_1\right)} = \frac{2}{\kappa \tilde{R}_1}\left(1 - A\tan\left[A\ln\left(\frac{\kappa \tilde{R}_1}{B}\right)\right]\right) \qquad [24]$$

The last relation gives the boundary condition for the overpotential 19 at $\tilde{r} = \tilde{R}_a$

$$\ln\left\{\frac{4A^2}{\kappa^2 \tilde{R}_a^2}\left(1 + \tan^2\left[A\ln\left(\frac{\kappa \tilde{R}_a}{B}\right)\right]\right)\right\} = \tilde{\eta}_c^{+,0} \qquad [25]$$

The Equations 23–25 determine the constants A, B and $\tilde{R}_1$; these three parameters, in turn, fully determine the solution of the problem:

$$\tilde{\eta}_c^+ = \begin{cases} \ln\left\{\frac{4A^2}{\kappa^2 \tilde{r}^2}\left(1 + \tan^2\left[A\ln\left(\frac{\kappa \tilde{r}}{B}\right)\right]\right)\right\}, & \tilde{R}_a \leq \tilde{r} \leq \tilde{R}_1 \\[2ex] \frac{K_0\left(\kappa \tilde{r}\right)}{K_0\left(\kappa \tilde{R}_1\right)}, & \tilde{R}_1 < \tilde{r} < \infty \end{cases}$$

$$[26]$$

Eqs. 23–25 have multiple roots, as they contain periodic functions. The physical solution provides the set $\{A, B, \tilde{R}_1\}$ with the minimal positive A; the other sets lead to unphysical local peaks of $\tilde{\eta}_c^+$ in the anode-free domain. Note that the case of the cathode of a finite radius $\tilde{R}_c$ leads to somewhat more complicated solutions listed in Appendix A.

Results and Discussion

Shapes of overpotential for different anode radii.— Numerical solution to the system 23–25 for the constants A, B and $\tilde{R}_1$ is obtained as following. Solving Eq. 24 for B we get

$$B = \kappa \tilde{R}_1 \exp\left(\frac{1}{A}\left[\arctan\left\{\frac{1}{A}\left(\frac{\kappa \tilde{R}_1 K_1\left(\kappa \tilde{R}_1\right)}{2K_0\left(\kappa \tilde{R}_1\right)} - 1\right)\right\}\right]\right) \quad [27]$$

Substituting 27 into Eqs. 23 and 25, we get a system of two equations for the parameters A and $\tilde{R}_1$. This system can be solved by standard numerical procedures utilizing Newton's method, taking A in the range of 0.25 to 1 and $\tilde{R}_1$ in the range of $1/\kappa$ to $2/\kappa$ as the initial guess. The parameter B is then calculated with Eq. 27. Note that a more accurate initial guess for A provides a function

$$A = \frac{\pi}{2}\left[\ln\left(\frac{29}{12(\kappa \tilde{R}_a)^{4/9}}\right)\right]^{-1}.$$

The solution 26 is valid outside the working cell area, in the anode-free domain $\tilde{r} \geq \tilde{R}_a$. Comparison of Eq. 26 to the numerical solution of the full problem, Eq. 9 for $0 \leq \tilde{r} < \infty$ is depicted in Figure 4. As can be seen, the analytical curves are very close to the numerical results (points). Note rapid decay of the overpotential close to the anode surface (Figure 4).

For the anode radii $\tilde{R}_a < 10$, the numerical solution is difficult to obtain due to a very steep gradient of $\tilde{\eta}_c^+$ near the anode edge. A key feature of this problem is that this gradient increases with the decrease of the anode radius. A more detailed view of the η_c^+ shapes, which illustrates this behavior is depicted in Figure 5a. Figure 5b shows the analytical curves in Figure 5a shifted along the $\tilde{r}$-axis in such a way, that the anode edges coincide. Note a faster decay of η_c^+ near the anode of a smaller radius. Qualitatively, this effect is similar to behavior of the Laplace potential between a charged axially-symmetric metal tip and a plane: the smaller the tip radius, the faster decays the potential
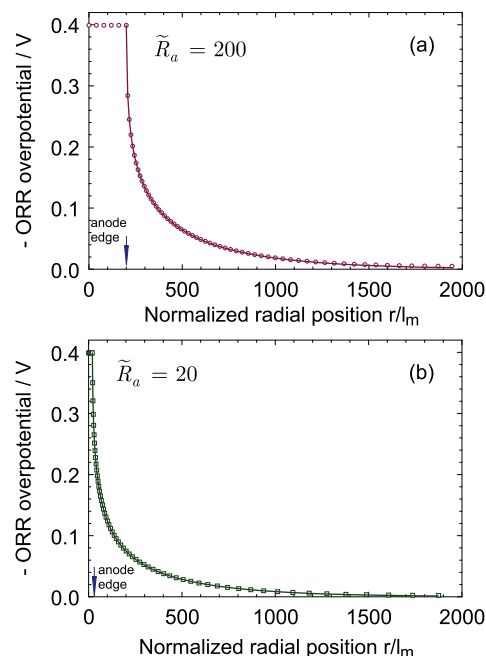

Figure 4. Numerical (points) and analytical (lines) shapes of the ORR overpotential for the dimensionless anode radius $\tilde{R}_a$ of (a) 200 and (b) 20. The "infinite" cathode radius is $\tilde{R}_c = 2000$. The points exhibit the numerical solution to the full problem 9, while the lines show Eq. 26, which is valid outside the anode. Parameters for the calculations are listed in Table I.

along the symmetry axis of the problem.[15] The main practical conclusion from Figure 5b is that in a cell with the smaller anode radius, the reference electrode can be positioned closer to the anode edge. This is discussed in detail in Positioning of the reference electrode section.
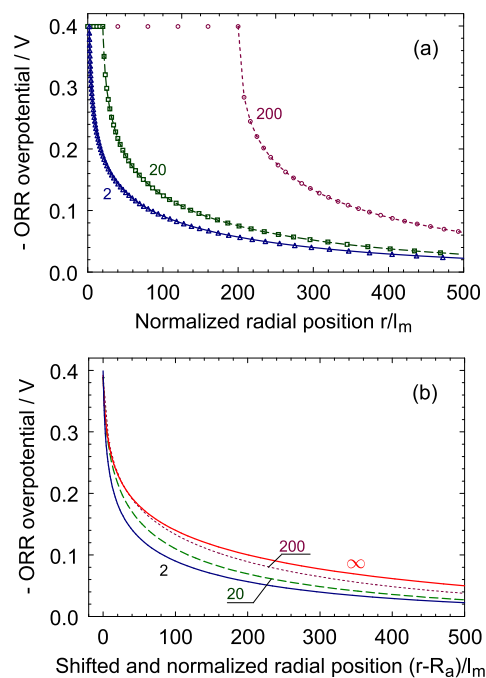

Figure 5. (a) Zoom of the curves in Figure 4 and the overpotential for the anode radius $\tilde{R}_a = 2$. (b) The analytical curves shown in (a) shifted in such a way that the anode edges coincide. Indicated are the dimensionless anode radii. Note faster decay of the ORR overpotential η_c^+ near the anode of a smaller radius. The symbol ∞ marks the shape of η_c^+ at the edge of the plane anode.[8]

Debye screening.— Consider the system of Equations 23, 24 and 25 for the constants A, B and $\tilde{R}_1$ and suppose that $\tilde{\eta}_c^{+,0} \to \infty$. It can be shown that A is bounded (Appendix B): $A \le M$, where M is some constant. Thus, the tan-function in Eq. 25 must be large; this means, that for $\tilde{\eta}_c^{+,0} \to \infty$ the argument of this function tends to $\pi/2$, and hence for large $\tilde{\eta}_c^{+,0}$ Eq. 25 can be replaced by

$$A \ln \left(\frac{\kappa \tilde{R}_a}{B} \right) = \frac{\pi}{2} \qquad [28]$$

With this, the parameters A, B and $\tilde{R}_1$ can be determined from the reduced system of Equations 23, 24 and 28, *which is independent of* $\tilde{\eta}_c^{+,0}$. It follows, that at large $\tilde{\eta}_c^{+,0}$, the long-range radial shape of the overpotential in Eq. 26 only weakly depends on its boundary value $\tilde{\eta}_c^{+,0}$.

Large overpotential means that $\tilde{\eta}_c^{+,0} \gg 1$. For the typical PEMFC parameters (Table I), this condition holds at very small cell currents (see above) i.e., for the typical cell current densities of 0.1 to 1 A cm^{-2}, the long-range shape of overpotential weakly depends on the cell current density. To illustrate this effect, Figure 6 shows comparison of the width of the ORR-dominated domain

$$\tilde{L}_{1,r} = \tilde{R}_1 - \tilde{R}_a \qquad [29]$$

determined from the reduced system 23, 24 and 28, to the exact value resulted from the system 23, 24 and 25. The two curves are very close to each other. Taking into account that $\tilde{R}_1$ is on the order of $1/\kappa$, this result is quite analogous to Debye screening in plasmas: at the distance on the order of $\tilde{\lambda}_D = 1/\kappa$, the charge of the macroscopic rod-like particle is screened, so that any variation of this charge is not "seen" at larger distances. Here, "screening" makes the behavior of the cathode overpotential at the distances $\tilde{r} > 1/\kappa$ only weakly dependent of the overpotential (or current) in the working domain of the cell. This effect can also be demonstrated in the case of the straight anode edge above the large cathode active area (Figure 1b). Calculations[8] have shown, that in this cell, the overpotential $\tilde{\eta}_c^+$ decays with the distance $\tilde{x}$ from the anode edge according to

$$\tilde{\eta}_c^+ = 2 \ln \left(\frac{1 + G \exp(-\kappa \tilde{x})}{1 - G \exp(-\kappa \tilde{x})} \right) \qquad [30]$$

In general, the constant G is determined from matching of Eq. 30 and the solution in the working cell area. However, as discussed above, in PEMFC, the cathode overpotentials at the anode edge and in the working domain are nearly the same, and we can determine G from the condition $\tilde{\eta}_c^+(0) = \tilde{\eta}^{+,0}$, where $x = 0$ is located at the straight edge of the anode (Figure 1b). Substituting this G into Eq. 30 and solving equation $\tilde{\eta}_c^+ = 1$, we find the distance $\tilde{L}_{1,x}$ where $\tilde{\eta}_c^+$ drops to
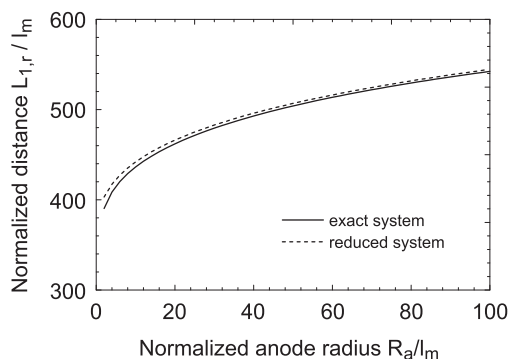

Figure 6. Solid line—the exact width of the ORR-dominated domain $\tilde{L}_{1,r} = \tilde{R}_1 - \tilde{R}_a$ vs. the anode radius $\tilde{R}_a$ for base-case set of parameters (Table I). Dashed line—the same width calculated from the reduced system of equations 23, 24 and 28, which is independent of the overpotential in the working cell area $\tilde{\eta}_c^{+,0}$ (i.e., it is independent of the cell current density).
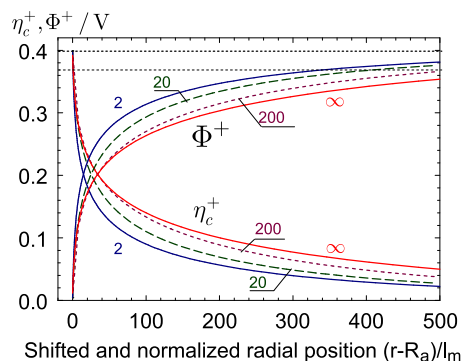

Figure 7. Analytical radial shapes of the positive ORR overpotential η_c^+ (cf. Figure 5b) and the respective shapes of the positive membrane potential Φ^+ for the indicated anode radii $\tilde{R}_a$.

unity:

$$\tilde{L}_{1,x} = \frac{1}{\kappa} \ln \left(\frac{\left(\exp\left(\frac{\tilde{\eta}^{+,0}}{2} \right) - 1 \right) \left(\exp\left(\frac{1}{2} \right) + 1 \right)}{\left(\exp\left(\frac{\tilde{\eta}^{+,0}}{2} \right) + 1 \right) \left(\exp\left(\frac{1}{2} \right) - 1 \right)} \right) \qquad [31]$$

For $\tilde{\eta}^{+,0} \gg 1$, this result simplifies to

$$\tilde{L}_{1,x} \simeq \frac{1}{\kappa} \ln \left(\frac{\exp\left(\frac{1}{2} \right) + 1}{\exp\left(\frac{1}{2} \right) - 1} \right) \simeq \frac{1.4}{\kappa} \qquad [32]$$

which is independent of $\tilde{\eta}_c^{+,0}$, i.e, independent of the cell current. This is a signature of Debye screening.

Positioning of the reference electrode.— In the remainder of this work, we will discuss the analytical curves $\tilde{\eta}_c^+(\tilde{r})$, as they practically coincide with the numerical solutions. Figure 7 shows the shapes of the positive membrane potential $\Phi^+ = -\Phi > 0$ for the same anode radii as in Figure 5b. The shapes of Φ^+ have been calculated using the dimensional versions of Eqs. 11, 26 and the parameters in Table I. As can be seen, at large $\tilde{r}$, Φ^+ tends to the limiting value $\Phi^{+,\infty} = \eta_c^{+,0}$. Indeed, subtracting the relations

$$\tilde{\eta}_c^{+,0} = \tilde{E}_{ORR}^{eq} - \tilde{\phi}_c - \tilde{\Phi}^{+,0}$$

$$\tilde{\eta}_c^{+,\infty} = \tilde{E}_{ORR}^{eq} - \tilde{\phi}_c - \tilde{\Phi}^{+,\infty} = 0$$

we get

$$\tilde{\eta}_c^{+,0} = \tilde{\Phi}^{+,\infty} - \tilde{\Phi}^{+,0} \simeq \tilde{\Phi}^{+,\infty} \qquad [33]$$

as in PEMFCs, $\tilde{\Phi}^{+,0} \simeq 0$, i.e., the membrane potential in the working domain is close to zero. Here, the superscript ∞ marks the values at $\tilde{r} \to \infty$.

As discussed above, Φ^+ corresponding to smaller anode radius tends to $\eta_c^{+,0}$ faster (Figure 7). This effect is illustrated in Figure 8, which shows the radial width of the ORR-dominated domain $\tilde{L}_{1,r}$, Eq. 29. The width $\tilde{L}_{1,r}$ increases with the anode radius $\tilde{R}_a$ (Figure 8). Due to Debye screening, the parameter $\tilde{L}_{1,r}$ weakly depends of the cell current density and the shapes of $\tilde{\eta}_c^+(\tilde{R}_a)$ and of $\tilde{L}_{1,r}(\tilde{R}_a)$ are governed mainly by the Debye parameter κ.

For further estimates we will assume that the reference electrode can be located at the distance $\tilde{L}_{1,r}$ from the anode edge. Figure 7 shows that this assumption provides 10%-accuracy of $\tilde{\eta}_c^+$ determination (the bottom straight dotted line). It is advisable to compare the distance $\tilde{L}_{1,r}$ to the analogous distance $\tilde{L}_{1,x}$, Eq. 32 for the straight anode edge geometry (Figure 8). Straight long-dashed lines in Figure 8 depict the value of $\tilde{L}_{1,x}$ for the two sets of parameters; $\tilde{L}_{1,x}$ is an asymptote to which the respective $\tilde{L}_{1,r}$ curve tends as $\tilde{R}_a \to \infty$. For small anode radii $\tilde{R}_a \lesssim 10$, the distance $\tilde{L}_{1,r}$ between the curved anode edge and the RE is at least twice smaller, than this distance $\tilde{L}_{1,x}$ for the
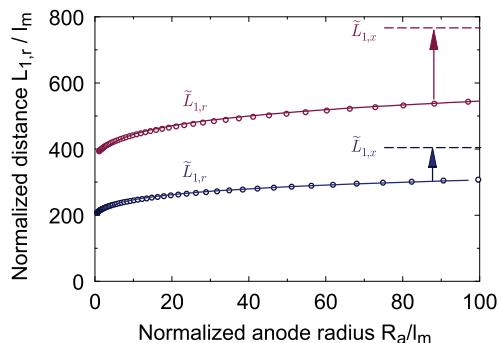
Figure 8. The width of the ORR-dominated domain $\tilde{L}_{1,r} = \tilde{R}_1 - \tilde{R}_a$ vs. the anode radius $\tilde{R}_a$. At the distance $\tilde{R}_1 - \tilde{R}_a$ from the anode edge, the ORR overpotential drops to the value of the Tafel slope b_{ox}, while the membrane potential Φ nearly reaches the value of the cathode overpotential η_c^0 in the working domain. Upper solid curve—the base-case set of parameters (Table I). Lower solid curve corresponds to $j_{ox}^0 = 6 \cdot 10^{-6}$ A cm^{-2}, $b_{ox} = 0.05$ V and to the cell potential of 0.65 V; the other parameters are those indicated in Table I. Open circles-the approximate fitting Equation 34. Long-dashed lines—the distance $\tilde{L}_{1,x}$, corresponding to the straight anode edge (see text).

straight anode edge (Figure 8). Note rapid decay of $\tilde{L}_{1,r}$ for the small anode radii (Figure 8); however, for $\tilde{R}_a \lesssim 1$, accuracy of the model decreases, as it ignores three-dimensional effects in a close proximity of the anode edge.

An approximate expression for the dependence $\tilde{L}_{1,r}(\tilde{R}_a)$ in the range $0 \le \kappa \tilde{R}_a \le 1$ is

$$\tilde{L}_{1,r} \simeq \frac{\pi}{2\kappa} \left[\ln \left(\frac{67}{18(\kappa \tilde{R}_a)^{7/45}} \right) \right]^{-1} \quad 0 \le \kappa \tilde{R}_a \le 1 \quad [34]$$

(Figure 8, open circles). In the dimensional form this equation reads

$$L_{1,r} \simeq \frac{\pi \lambda_D}{2} \left[\ln \left(\frac{67}{18(R_a/\lambda_D)^{7/45}} \right) \right]^{-1}, \quad [35]$$

where λ_D is given by Eq. 14. Eq. 35 can be used for engineering estimates of the gap distance L_{gap} between the anode tip of a radius R_a and the reference electrode. If high accuracy of measurements is needed, taking $L_{\text{gap}} \simeq 3L_{1,r}$ is recommended.

Figure 9 shows possible configurations of a fuel cell with the reference electrode. Figure 9a displays the reference electrode in the system with the straight anode edge. In this case, the distance $L_{\text{gap}} \simeq 3\lambda_D$, as reported in.[8] Figure 9b exhibits the case of the circular anode; here the distance $L_{\text{gap}} \simeq 3L_{1,r}$, where $L_{1,r}$ is given by Eq. 35. Note that here L_{gap} is smaller, than in Figure 9a. Figure 9c shows the anode edge with the sharp tip; this tip provides a rapid growth of Φ^+ with the distance from the tip. Thus, the reference electrode can be positioned closer to the tip not sacrificing the accuracy of measurements. L_{gap} in Figure 9c can be estimated from Eq. 35, taking R_a equal to the radius of tip curvature.

From Eq. 35 it is evident, that Eq. 16 is redundant. Eq. 16 describes a minimal size of the anode-free domain for the system with the straight anode edge. In the system with the curved anode edge, the size of the anode-free domain must obey to

$$L_{\text{gap}} \simeq 3L_{1,r} \quad [36]$$

where $L_{1,r}$ is given by Eq. 35. Clearly, at the distance on the order of 36, the local cathode overpotential drops to a vanishingly small value, and the model above is applicable.

Discussion.— Eq. 12 describes a kind of "electrostatics" for overpotential distribution in the anode-free domain. Thinness of the membrane and its large in-plane size makes this electrostatics almost two-dimensional. Numerical solutions to a fully 2D analog of Eq. 12 could give more insights into an optimal shape of the anode tip for positioning the reference electrode. However, due to very large gradients of
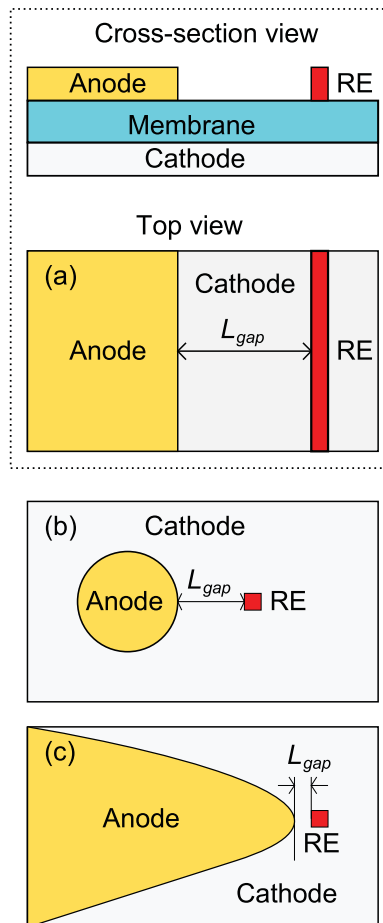

Figure 9. Schematic of the reference electrode (RE) positioning for different anode geometries. (a) The straight anode edge, (b) the circular anode (c) the anode with the curved tip of a small radius. The smaller the tip radius, the closer to the tip can be located the RE.

potentials at the anode edge, fully 2D calculations might require special numerical techniques.

In the anode-free domain, hydrogen is not needed. In the absence of electroosmotic flux of water, the membrane in this domain can be humidified by the backflux of water from the cathode side. If, for technological reasons, a hydrogen flow field "covers" the anode-free domain, the H$_2$ crossover through the membrane can be blocked by applying some polymer material between the anode flow field and membrane.

In general, in the anode-free domain, the decaying cathode overpotential may accelerate carbon corrosion reaction (CCR) on the cathode side. The overpotential for CCR is $\eta_c^{CCR} = \phi_c - \Phi - E_{CCR}^{eq}$, where $E_{CCR}^{eq} \simeq 0.207$ V is the CCR equilibrium potential. Far from the anode edge, we have $\Phi \simeq \eta_c^0$, and thus $\eta_c^{CCR} \simeq \phi_c - \eta_c^0 - E_{CCR}^{eq}$. With the typical $\phi^c \simeq 0.6$ V and $\eta_c^0 \simeq -0.3$ V, we find $\eta_c^{CCR} \simeq 0.7$ V. In a true OCV state of a PEMFC, this overpotential is about 0.9 to 1 V, which induces much higher rate of corrosion. In addition, there is no counter electrode in the anode-free domain, and in order to be captured in the ORR, the proton produced in the CCR must travel quite a large distance along the cathode to the point, where the local ORR overpotential is sufficiently large. Due to a relatively large ohmic resistance of the membrane phase in the CCL, this proton transport would lower the overall rate of corrosion.

Conclusions

A model for the radial distribution of the membrane potential Φ and of the ORR overpotential η_c in a PEM fuel cell with the concentric

small anode and large cathode is developed. In the anode-free area of the cell, the model reduces to the axially symmetric Poisson–Boltzmann equation for η_c. An approximate analytical solution for this equation is constructed. A feature of this problem is weak dependence of the long-range shape of $\eta_c(r)$ on the value of η_c^0, where η_c^0 is the ORR overpotential in the working domain of the cell. This effect is quite analogous to Debye screening in plasmas.

The solution shows rapid convergence of Φ to the value of η_c^0 with the distance from the anode edge r. Moreover, the smaller the anode radius, the faster tends Φ to η_c^0 with r. This result shows that the reference electrode measuring $\Phi \simeq \eta_c^0$ can be located closer to the anode edge, if the latter is curved.

Appendix A: The Case of a Finite Cathode Radius

The model above can be modified for the cathode of the finite radius $\tilde{R}_c$. In this case, the long-range problem Eq. 12 reads

$$\frac{1}{\tilde{r}}\frac{d}{d\tilde{r}}\left(\tilde{r}\frac{d\tilde{\eta}_c^+}{d\tilde{r}}\right) = \kappa^2\tilde{\eta}_c^+, \quad \left.\frac{d\tilde{\eta}_c^+}{d\tilde{r}}\right|_{\tilde{r}=\tilde{R}_c} = 0 \qquad [A1]$$

Solution to Eq. A1 is

$$\tilde{\eta}_{c,L}^+ = C\left(\frac{I_1\left(\kappa\tilde{R}_c\right)}{K_1\left(\kappa\tilde{R}_c\right)}K_0\left(\kappa\tilde{r}\right) + I_0\left(\kappa\tilde{r}\right)\right), \quad \tilde{\eta}_{c,L}^+ \ll 1 \qquad [A2]$$

where I and K are the modified Bessel functions of the first and second kind, respectively and C is the constant, which is determined from the condition $\tilde{\eta}_{c,L}^+(1) = \tilde{R}_1$. This yields

$$\tilde{\eta}_{c,L}^+ = \frac{I_1\left(\kappa\tilde{R}_c\right)K_0\left(\kappa\tilde{r}\right) + K_1\left(\kappa\tilde{R}_c\right)I_0\left(\kappa\tilde{r}\right)}{I_1\left(\kappa\tilde{R}_c\right)K_0\left(\kappa\tilde{R}_1\right) + K_1\left(\kappa\tilde{R}_c\right)I_0\left(\kappa\tilde{R}_1\right)} \qquad [A3]$$

which replaces Eq. 22. The solution for the short-range problem remains the same, Eq. 19. Continuity of the first derivatives of the short- and long-range solutions at $\tilde{r} = \tilde{R}_1$ gives an equation

$$\frac{I_1\left(\kappa\tilde{R}_c\right)K_1\left(\kappa\tilde{R}_1\right) - K_1\left(\kappa\tilde{R}_c\right)I_1\left(\kappa\tilde{R}_1\right)}{I_1\left(\kappa\tilde{R}_c\right)K_0\left(\kappa\tilde{R}_1\right) + K_1\left(\kappa\tilde{R}_c\right)I_0\left(\kappa\tilde{R}_1\right)} = \frac{2}{\kappa\tilde{R}_1}\left(1 - A\tan\left[A\ln\left(\frac{\kappa\tilde{R}_1}{B}\right)\right]\right) \quad [A4]$$

which replaces Eq. 24. Thus, the full solution of the problem is now given by

$$\tilde{\eta}_c^+ = \begin{cases} \ln\left\{\frac{4A^2}{\kappa^2\tilde{r}^2}\left(1 + \tan^2\left[A\ln\left(\frac{\kappa\tilde{r}}{B}\right)\right]\right)\right\}, & \tilde{R}_a \le \tilde{r} \le \tilde{R}_1 \\[2ex] \frac{I_1\left(\kappa\tilde{R}_c\right)K_0\left(\kappa\tilde{r}\right) + K_1\left(\kappa\tilde{R}_c\right)I_0\left(\kappa\tilde{r}\right)}{I_1\left(\kappa\tilde{R}_c\right)K_0\left(\kappa\tilde{R}_1\right) + K_1\left(\kappa\tilde{R}_c\right)I_0\left(\kappa\tilde{R}_1\right)}, & \tilde{R}_1 < \tilde{r} \le \tilde{R}_c \end{cases} \qquad [A5]$$

where A, B and $\tilde{R}_1$ are determined by the system of Equations 23, A4 and 25.

Appendix B: Proof that the Parameter A is Bounded

Solving Eq. 24 for $\tan\left[A\ln\left(\kappa\tilde{R}_1/B\right)\right]$, and substituting the result into Eq. 23, we come to

$$\frac{4A^2}{\kappa^2\tilde{R}_1^2} + \frac{4}{\kappa^2\tilde{R}_1^2}\left(1 - \frac{\kappa\tilde{R}_1K_1\left(\kappa\tilde{R}_1\right)}{2K_0\left(\kappa\tilde{R}_1\right)}\right) = \exp(1) \qquad [B1]$$

Let $\tilde{\eta}_c^{+,0} \to \infty$ and suppose that $A \to \infty$. Clearly, in order for Eq. B1 be satisfied, $\tilde{R}_1$ must also tend to infinity, otherwise the first term on the left side would be infinite. With $\kappa\tilde{R}_1 \to \infty$, we have $K_1\left(\kappa\tilde{R}_1\right)/K_0\left(\kappa\tilde{R}_1\right) = 1$, the second term on the left side of Eq. B1 tends to zero, and from Eq. B1 it follows that

$$\frac{2A}{\kappa\tilde{R}_1} = \sqrt{\exp(1)}, \quad A \sim \tilde{R}_1 \to \infty \qquad [B2]$$

Using this relation in Eq. 27, we find

$$B = \kappa\tilde{R}_1, \quad A \sim \tilde{R}_1 \to \infty \qquad [B3]$$

Finally, using this B in Eq. 25, we get

$$\ln\left(\frac{4A^2}{\kappa^2\tilde{R}_a^2}\right) + \ln\left(1 + \tan^2\left[A\ln\left(\frac{\tilde{R}_a}{\tilde{R}_1}\right)\right]\right) = \tilde{\eta}_c^{+,0} \qquad [B4]$$

With $\tilde{\eta}_c^{+,0} \to \infty$, the minimal positive root A of this equation always exists in the range

$$0 < A < \frac{\pi}{2\ln\left(\tilde{R}_1/\tilde{R}_a\right)}$$

as $\tilde{R}_1 > \tilde{R}_a$. Thus, A is bounded, which contradicts to the assumption $A \to \infty$. From Eq. B1 it follows, that if A is bounded, $\tilde{R}_1$ is also bounded.

List of Symbols

~	Marks dimensionless variables
A	Dimensionless constant
B	Dimensionless constant
b	Tafel slope, V
E^{eq}	Equilibrium half-cell potential, V
F	Faraday constant
G	Dimensionless constant in Eq. 30
J	Mean current density in the working domain, A cm^{-2}
j_a	Local proton current density on the anode side, A cm^{-2}
j_c	Local proton current density on the cathode side, A cm^{-2}
j_{hy}	HOR exchange current density, A cm^{-2}
j_{hy}^0	HOR exchange current density in the center of the working domain, A cm^{-2}
j_{ox}^0	ORR exchange current density, A cm^{-2}
L_{gap}	Gap length between the edge of the working electrode and the reference electrode, cm
$L_{1,x}$	Distance from the straight anode edge, to the point where $\tilde{\eta}_c^+ = 1$, cm
$L_{1,r}$	Radial distance from the circular anode edge, to the point where $\tilde{\eta}_c^+ = 1$, cm
l_m	Membrane thickness, cm
R	Gas constant
R_1	Radial position where $\tilde{\eta}_c^+ = 1$, cm
R_a	Anode radius, cm
R_c	Cathode radius, cm
r	Radial position, cm
y	Coordinate through the membrane, cm

Greek

α	Transfer coefficient of the ORR rate-determining step
η	Local overpotential, V
$\eta_c^{+,0}$	Positive cathode overpotential at $r = 0$, V
κ	Dimensionless Debye parameter, Eq. 13
λ_D	Debye length, cm, Eq. 14
σ_m	Membrane ionic conductivity, Ω^{-1} cm^{-1}
Φ	Membrane potential, V
Φ^+	Positive membrane potential, V
$\Phi^{+,\infty}$	Positive membrane potential at $r \to \infty$, V
ϕ	Carbon phase (electrode) potential, V

Subscripts

1	Radial position, where $\tilde{\eta}_c^+ = 1$
a	Anode
c	Cathode
HOR	Hydrogen oxidation reaction
hy	Hydrogen
m	Membrane
ORR	Oxygen reduction reaction
ox	Oxygen
r	System with radial geometry
ref	Reference electrode
t	Catalyst layer
x	System with the straight anode edge

Superscripts

+	Positive value
0	Center of the working electrodes, $\tilde{r} = 0$
∞	Infinite radial distance

References

1. J. Giner, *J. Electrochem. Soc.*, **111**, 376 (1964).
2. A. C. West and J. Newman, *J. Electrochem. Soc.*, **136**, 3755 (1989).

3. J. Winkler, P. V. Hendriksen, N. Bonanos, and M. Mogensen, *J. Electrochem. Soc.*, **145**, 1184 (1998).
4. S. B. Adler, B. T. Henderson, M. A. Wilson, D. M. Taylor, and R. E. Richards, *Solid State Ionics*, **134**, 35 (2000).
5. S. B. Adler, *J. Electrochem. Soc.*, **149**, E166 (2002).
6. J. Rutman and I. Riess, *Electrochimica Acta*, **52**, 6073 (2007).
7. D. Gerteisen, *J. Appl. Electrochem.*, **37**, 1447 (2007).
8. A. A. Kulikovsky and P. Berg, *J. Electrochem. Soc.*, **162**, F843 (2015).
9. A. A. Kulikovsky, *SIAM J. Appl. Math.*, **70**, 531 (2009).
10. A. A. Kulikovsky and P. Berg, *ECS Electrochem. Lett.*, **9**, F64 (2013).
11. M. Gouy, *J. Phys. Radium (Paris)*, **9**, 457 (1910).
12. D. L. Chapman, *Philos. Mag.*, **6**, 475 (1913).
13. L. G. Dyachkov, *Techn. Phys. Lett.*, **31**, 204 (2005).
14. E. K. Zholkovskij, S. S. Dukhin, N. A. Mishchuk, J. H. Masliyah, and J. Czarnecki, *Colloids and Surfaces A: Physicochem. Eng. Aspects*, **192**, 235 (2001).
15. G.-S. Cho, D.-E. Kim, and S.-O. Kang, *J. Phys. D: Appl. Phys.*, **23**, 85 (1990).